Cell Polarity and Movement with Reaction-Diffusion and Moving Boundary: Rigorous Model Analysis and Robust Simulations

Shuang Liu * Li-Tien Cheng † Bo Li ‡ September 13, 2023

Abstract

Cell polarity and movement are fundamental to many biological functions. Experimental and theoretical studies have indicated that interactions of certain proteins lead to the cell polarization which plays a key role in controlling the cell movement. We study the cell polarity and movement based on a class of biophysical models that consist of reaction-diffusion equations for different proteins and the dynamics of moving cell boundary. Such a moving boundary is often simulated by a phase-field model. We first apply the matched asymptotic analysis to give a rigorous derivation of the sharp-interface model of the cell boundary from a phase-field model. We then develop a robust numerical approach that combines the level-set method to track the sharp boundary of a moving cell and accurate discretization techniques for solving the reaction-diffusion equations on the moving cell region. Our extensive numerical simulations predict the cell polarization under various kinds of stimulus, and capture both the linear and circular trajectories of a moving cell for a long period of time. In particular, we have identified some key parameters controlling different cell trajectories that are less accurately predicted by reduced models. Our work has linked different models and also developed tools that can be adapted for the challenging three-dimensional simulations.

Key words and phrases: cell polarity, cell movement, reaction-diffusion equations, interface dynamics, matched asymptotic analysis, the level-set method.

1 Introduction

Cell motility is fundamental to many biological functions such as immune response, morphogenesis, cancer metastasis, and wound healing, and yet it is extremely complicated [7]. The movement of a eukaryotic cell crawling on a surface is a complex process, involving protrusion, retraction, and adhesion, exhibiting complex geometrical shapes and motion trajectories. Cell polarity, the spatially inhomogeneous distribution of different biomolecules such as proteins Rho GTPases inside a cell, resulting from biochemical interactions of biomolecules inside the cell, plays a crucial role in the cell movement [24, 32, 40]. As cell polarity and movement involve multiple spatio-temporal scales and many-body interactions, understanding rigorously such complex processes is challenging.

^{*}Department of Mathematics, University of California, San Diego, 9500 Gilman Drive, La Jolla, California 92093-0112, United States. Email: shl083@ucsd.edu

[†]Department of Mathematics, University of California, San Diego, 9500 Gilman Drive, La Jolla, California 92093-0112, United States. Email: l3cheng@ucsd.edu

[‡]Department of Mathematics and Quantitative Biology Ph.D. Program, University of California, San Diego, 9500 Gilman Drive, La Jolla, California 92093-0112, United States. Email: bli@ucsd.edu

Recent years have seen the theoretical and computational developments in studying cell polarity and motility [8,31,32]. Among different approaches, continuum models with reaction-diffusion equations and moving boundaries provide efficient simulation tools to understand the key mechanisms in cell polarity and movement [9-11,15,34,41,43-45,45,52,54]. An advantage of such modeling is that the motion of cell boundary, which is directly connected to the reaction and diffusion of different biomolecules inside the cell, can be simulated and analyzed to link the molecular basis for the cell polarity to the macroscopic cell movement, and to identify the key parameters that control the cell polarization and movement.

In this work, we study the cell polarity and movement with a class of models that have been proposed in Mori et al. [33, 34], Shao et al. [44], and Camley et al. [10, 11, 45]. In such models, the boundary of a moving cell is determined completely by its normal velocity, i.e., the normal component of the velocity. In addition to geometrical effects, such normal velocity is controlled by the biochemical interactions of different proteins such as Rho GTPases. For many different types of cells, each Rho GTPase cycles between an active, membrane-bound form and an inactive, cytosolic GDP-bound form; cf. Figure 1.1. The concentration of the active Rho GTPases is high in the front of a moving cell, while the inactive Rho GTPases diffuse fast and tend to be homogeneously distributed. Mori et al. [33] propose the wave-pinning mechanism for the cell polarization: the reaction and diffusion of the active and inactive Rho GTPases with bistable kinetics and the mass conservation of these proteins lead to the formation of an interface inside a cell. The interface separates a high from a low concentration of active Rho-GTPase proteins, and the propagation of such interface drives the cell polarization that reaches a steady state eventually, as the wave is pinned down. Camley et al. [11,45] reduce the two-species (active form and inactive form of Rho GTPase proteins) model proposed in [33] to a single-species model, and also numerically simulated the cell polarization and movement using a phase-field method, but carried out analysis with a sharp-interface description of the cell boundary motion. Simulations by Camley et al. [11] predict linear and circular trajectories as a result of the wave-pinning dynamics.

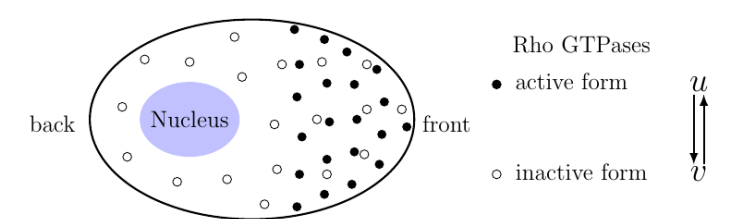


Figure 1.1: Schematic view of a cell moving on a substrate. The active Rho GTPase is rich in the front, while the inactive GDP-bound Rho GTPases diffuse fast and are more homogeneously distributed. The concentrations of these proteins are denoted by u and v, respectively.

To be specific, let us consider a moving cell confined spatially in a bounded region $\Omega \subset \mathbb{R}^d$ (d=2 or 3). Let us denote the cell boundary by $\Gamma(t)$ at time t and assume it moves with the normal velocity V = V(x,t) for each point $x \in \Gamma(t)$, where the normal direction points from the interior to the exterior of the cell. The cell boundary $\Gamma(t)$ separates the region Ω into the cell region, denoted $\Omega^+(t)$, from the outer region, denoted $\Omega^-(t)$. We denote by u=u(x,t) and v=v(x,t) the concentrations of the active and inactive Rho GTPases, respectively, inside the cell. Extended from the one-dimensional model [33] (cf. also [44]), our model of an underlying moving cell is governed by the following system of equations and boundary conditions:

$$\tau V = \alpha u - \beta - \gamma H \qquad \text{for } x \in \Gamma(t) \text{ and } t > 0, \tag{1.1}$$

$$\tau V = \alpha u - \beta - \gamma H \qquad \text{for } x \in \Gamma(t) \text{ and } t > 0,$$

$$\partial_t u = D_u \Delta u + f(u, v) \qquad \text{for } x \in \Omega^+(t) \text{ and } t > 0,$$

$$(1.1)$$

$$\partial_t v = D_v \Delta v - f(u, v)$$
 for $x \in \Omega^+(t)$ and $t > 0$, (1.3)

$$\partial_n u = \partial_n v = 0$$
 for $x \in \Gamma(t)$ and $t > 0$, (1.4)

where

$$f(u,v) = -ku(u - 0.5c)(u - Cv). \tag{1.5}$$

In (1.1), τ is the friction coefficient, α and β are the coefficients of F-actin extension and myosin retraction, respectively, γ is the surface tension constant, and H is the mean curvature of the cell boundary $\Gamma(t)$ (positive for a spherical boundary). In (1.2) and (1.3), D_u and D_v are the diffusion constants for u and v, respectively. We shall consider the regime that $D_v \gg D_u$. In the reaction term f(u,v) defined in (1.5), k is the reaction rate relative to an average cell motility, c is a constant value of concentration u, and C is a unitless conversion parameter. Note that our 0.5c is the quantity h in [11,33]. It represents an unstable state of concentration u whose kinetics is governed by f(u,v) with a constant v value. As u increases or decreases across this value 0.5c, the region of the cell front decreases or increases in size (cf. Figure 1.1) due to the mass conservation and fast diffusion of v, and hence the speed of the moving front changes, providing possibility of cell rotation; cf. [11,33,34] for more details. Estimated values of these parameters are given in Table 3 in section 4. Note that the total mass

$$M = \int_{\Omega^{+}(t)} [u(x,t) + v(x,t)] dx$$
 (1.6)

is a constant with respect to time t.

Assuming that $D_v \gg D_u$ and hence that approximately v = v(t) is spatially homogeneous, Camley et al. [11] propose and study the following single-species model, reduced from the two-species model (1.1)–(1.4):

$$\tau V = \alpha u - \beta - \gamma H \qquad \text{for } x \in \Gamma(t) \text{ and } t > 0, \tag{1.7}$$

$$\partial_t u = D_u \Delta u + f(u, \bar{v}) \qquad \text{for } x \in \Omega^+(t) \text{ and } t > 0, \tag{1.8}$$

$$\partial_n u = 0$$
 for $x \in \Gamma(t)$ and $t > 0$, (1.9)

where $\bar{v} = \bar{v}(t)$ is determined by the mass conservation (1.6), given by

$$\bar{v}(t) = \frac{1}{\operatorname{Area}(\Omega^+(t))} \left(M - \int_{\Omega^+(t)} u(x,t) \, dx \right).$$

To efficiently track the moving cell boundary in computer simulations, Shao et al. [43, 44] and Camley et al. [9–11] have developed a phase-field model. In such a model, the moving cell boundary is described by a continuous function, often called a phase field, that takes the value 1 in the cell region and 0 otherwise, and smoothly changes its value from 0 to 1 in a thin transition layer, representing a diffuse cell boundary. Let us denote by $\phi_{\varepsilon} = \phi_{\varepsilon}(x,t)$ ($x \in \Omega, t \geq 0$) such a phase-field function, where $\varepsilon \in (0,1)$ is a small parameter and t represents time. Let us also denote by $u_{\varepsilon} = u_{\varepsilon}(x,t)$ and $v_{\varepsilon} = v_{\varepsilon}(x,t)$ the concentrations of the two different proteins, respectively, as described in (1.2) and (1.3). Note that these functions are now extended to the entire region Ω . The phase-field model that corresponds to the system of equations (1.1)–(1.4), which shall be called a sharp-interface model, is then given by

$$\tau \partial_t \phi_{\varepsilon} = (\alpha u_{\varepsilon} - \beta) |\nabla \phi_{\varepsilon}| + \gamma \left[\Delta \phi_{\varepsilon} - \frac{1}{\varepsilon^2} W'(\phi_{\varepsilon}) \right] \quad \text{in } \Omega \times (0, \infty), \tag{1.10}$$

$$\partial_t(\phi_{\varepsilon}u_{\varepsilon}) = \nabla \cdot D_u(\phi_{\varepsilon}\nabla u_{\varepsilon}) + f(u_{\varepsilon}, v_{\varepsilon}) \quad \text{in } \Omega \times (0, \infty), \tag{1.11}$$

$$\partial_t(\phi_{\varepsilon}v_{\varepsilon}) = \nabla \cdot D_v(\phi_{\varepsilon}\nabla v_{\varepsilon}) - f(u_{\varepsilon}, v_{\varepsilon}) \quad \text{in } \Omega \times (0, \infty), \tag{1.12}$$

$$\phi_{\varepsilon} = u_{\varepsilon} = v_{\varepsilon} = 0 \quad \text{in } \partial\Omega \times [0, \infty),$$

$$(1.13)$$

where all the parameters and the function f are the same as above, and W = W(u) is a double-well potential given specifically by

$$W(u) = 18u^2(1-u)^2 \qquad \forall u \in \mathbb{R}. \tag{1.14}$$

We remark that the phase-field modeling approach has been widely used to study many interfacial problems arising from various scientific areas, such as materials physics, complex fluids, and biomembranes; cf. e.g., [2-6, 13, 19, 23, 25, 48] and the references therein. In such an approach, a phase field ϕ that minimizes the energy

$$E_{\varepsilon}[\phi] = \int \left[\frac{\varepsilon}{2} |\nabla \phi|^2 + \frac{1}{\varepsilon} W(\phi) \right] dx,$$

with W given in (1.14) and $0 < \varepsilon \ll 1$, approximates the characteristic function of the region interior to an underlying closed, sharp interface, and the corresponding value $E_{\varepsilon}[\phi]$ approximates the surface area [30,47]. Note that the γ -term in (1.10) is the surface tension force, given exactly by $-\gamma \delta_{\phi} E_{\varepsilon}[\phi]$, where $\delta_{\phi} E_{\varepsilon}$ denotes the first variation of the functional E_{ε} . The phase-field or diffuse-interface approach has been used to study numerically problems with moving boundaries of complex geometries or with singularities; cf. e.g., [1,14,27,50]. While such an approach can handle topological changes (such as breaking up and merging) of interfaces, care needs to be taken in the choice of the modeling parameter ε that characterizes the width of the diffuse interface and the size h of an underlying finite element mesh or finite difference grid to achieve optimal convergence rate.

In this work, we study the reaction-diffusion moving boundary model to understand the mechanisms of cell polarization and movement, and the cooperation of these two processes. Our goal is twofold. One is to understand the differences between some of the existing models and make connections of such models. The other is to develop robust computational tools for long-time accurate and efficient simulations of cell movement. Specifically:

- (1) We derive rigorously the sharp-interface, reaction-diffusion moving boundary model (1.1)–(1.4) from the phase-field model (1.10)–(1.13), using the matched asymptotic analysis. Our derivation justifies the phase-field model, though it does not prove the convergence as the parameter $\varepsilon \to 0$ due to the assumptions made in the analysis on the phase-field profile.
- (2) We develop a robust computational program that combines the level-set method and high-accurate discretization method for solving reaction-diffusion equations on a moving cell region and for tracking the moving cell boundary. We test our numerical methods. Our level-set method is based on the sharp-interface formulation (cf. (1.1)–(1.4) and (1.7)–(1.9)). It avoids the use of a very fine grid necessary to resolve a fine interfacial structure as in the phase-field method.
- (3) We apply our numerical methods and algorithms to conduct a series of computer simulations for the cell polarization and movement. We try to answer several questions: How does a cell respond to an external stimulus to polarize itself and then to move around? How does a cell keep different kinds of trajectories, such as a linear or a circular trajectory, for a very long time? Our computational analysis predicts several important parameters, such as a finite diffusion constant (instead of taking it to be infinite in a reduced model), the surface tension constant, and the threshold concentration of an active Rho GTPase protein, control partially the cell movement.

Our computational tools prepare us well for future, large-scale three-dimensional simulations of the cell movement, which are currently lacking in the field.

The paper is organized as follows. In section 2, we use the method of matched asymptotic analysis to derive the sharp-interface limit, the system (1.1)–(1.4), from the phase-field reaction-diffusion moving boundary model (1.10)–(1.13). In section 3, we describe a robust and accurate numerical method that combines a high-order finite difference discretization technique and a level-set method for the simulation of a moving cell. In section 4, we show our numerical simulations and analyze our results with various settings. Finally, in section 5, we draw our conclusions and discuss several issues for further studies.

2 From Phase-Field to Sharp-Interface Model

In this section, we carry out the matched asymptotic analysis [16–18, 26, 39, 42] to derive the sharp-interface model (1.1)–(1.4) from the phase-field model (1.10)–(1.13). Specifically, we show that as $\varepsilon \to 0$ the solution ϕ_{ε} converges to the characteristic function of the cell region $\Omega^{+}(t)$, the normal velocity of the cell boundary $\Gamma(t) = \partial \Omega^{+}(t)$ is given by (1.1), and the solutions u_{ε} and $\varepsilon_{\varepsilon}$ converge to the solutions to (1.2)–(1.4).

We shall analyze the following more general phase-field model in the setting of three-dimensional space:

$$\partial_t \phi_{\varepsilon} = h(u_{\varepsilon}, v_{\varepsilon}) |\nabla \phi_{\varepsilon}| + \gamma \left[\Delta \phi_{\varepsilon} - \frac{1}{\varepsilon^2} W'(\phi_{\varepsilon}) \right] \quad \text{in } \Omega \times (0, \infty), \tag{2.1}$$

$$\partial_t(\phi_{\varepsilon}u_{\varepsilon}) = \nabla \cdot D_1(\phi_{\varepsilon}\nabla u_{\varepsilon}) + f(u_{\varepsilon}, v_{\varepsilon}) \quad \text{in } \Omega \times (0, \infty), \tag{2.2}$$

$$\partial_t(\phi_{\varepsilon}v_{\varepsilon}) = \nabla \cdot D_2(\phi_{\varepsilon}\nabla v_{\varepsilon}) + g(u_{\varepsilon}, v_{\varepsilon}) \quad \text{in } \Omega \times (0, \infty), \tag{2.3}$$

$$\phi_{\varepsilon} = u_{\varepsilon} = v_{\varepsilon} = 0 \quad \text{in } \partial\Omega \times [0, \infty).$$
 (2.4)

Here, $\Omega \subset \mathbb{R}^3$ is a smooth and bounded domain, $\varepsilon \in (0,1)$ is a small parameter, $\gamma > 0$, $D_1 > 0$, and $D_2 > 0$ are all constants, and f, g, and h are all smooth and bounded two-variable functions. The double-well function W is defined in (1.14). Note that the analysis for the single-species system (1.7)–(1.9) or for a two-dimensional setting is similar.

Initial formation of a diffuse cell boundary. We assume the following expansions:

$$\phi_{\varepsilon}(x,t) = \phi_0(x,\tau) + \varepsilon\phi_1(x,\tau) + \varepsilon^2\phi_2(x,\tau) + \cdots,$$

$$u_{\varepsilon}(x,t) = u_0(x,\tau) + \varepsilon u_1(x,\tau) + \varepsilon^2 u_2(x,\tau) + \cdots,$$

$$v_{\varepsilon}(x,t) = v_0(x,\tau) + \varepsilon v_1(x,\tau) + \varepsilon^2 v_2(x,\tau) + \cdots,$$

where $\tau = \tau(t, \varepsilon)$ is a time variable that can be different from the regular time variable t, and all the functions $\phi_i = \phi_i(x, \tau)$, $u_i = u_i(x, \tau)$, and $v_i = v_i(x, \tau)$ (i = 0, 1, ...) are smooth and bounded in Ω , satisfying the boundary conditions $\phi_i = u_i = v_i = 0$ on $\partial\Omega$; cf. (2.4).

Considering a fast time scale $\tau = t/\varepsilon^2$, we have $\partial_t = \varepsilon^{-2}\partial_{\tau}$. Plugging the above expressions of ϕ_{ε} , u_{ε} , and v_{ε} into (2.1), using Taylor's expansion, and comparing terms of the leading orders $O(\varepsilon^{-2})$ and $O(\varepsilon^{-1})$, respectively, we obtain that

$$O(\varepsilon^{-2}): \quad \partial_{\tau}\phi_0 = -\gamma W'(\phi_0) \quad \text{and} \quad O(\varepsilon^{-1}): \quad \partial_{\tau}\phi_1 = -\gamma W''(\phi_0)\phi_1.$$

Since W'(s) = 0 if and only if s = 0, 1/2, or 1, with 0 and 1 being local minima of W and 1/2 being a local maximum of W, given any point $x \in \Omega$ and any initial data $\phi_0(x,0) \neq 1/2$, $\phi_0(x,\tau) \to 0$ or 1 exponentially as $\tau \to \infty$. Once ϕ_0 falls into $(-\infty, (3-\sqrt{3})/6) \cup ((3+\sqrt{3})/6, \infty)$, the convex region of W, then $\phi_1(x,\tau) \to 0$ exponentially as $\tau \to \infty$. If we consider the next fast time scale $\tau = t/\varepsilon$, then we have $\partial_t = \varepsilon^{-1}\partial_\tau$. Similar calculations lead to the leading-order equations

$$O(\varepsilon^{-2}): W'(\phi_0) = 0$$
 and $O(\varepsilon^{-1}): \partial_{\tau}\phi_0 = -\gamma W''(\phi_0)\phi_1.$

Again, we see that $\phi_0 = 0$, 1/2, or 1, and since $W''(\phi_0) \neq 0$, we have $\phi_1 = 0$. Results are the same if we consider the regular time scale $\tau = t$.

We can therefore assume that the region Ω is divided by the phase-field function ϕ_{ε} into an outer region $O_{\varepsilon}(t) := \Omega_{\varepsilon}^{-}(t) \cup \Omega_{\varepsilon}^{+}(t)$, where

$$\Omega_{\varepsilon}^{-}(t) = \{x \in \Omega : \phi_{\varepsilon}(x,t) = O(\varepsilon^{2})\} \quad \text{and} \quad \Omega_{\varepsilon}^{+}(t) = \{x \in \Omega : \phi_{\varepsilon}(x,t) = 1 + O(\varepsilon^{2})\},$$

and an inner region $I_{\varepsilon}(t) := \Omega \setminus O_{\varepsilon}(t)$, where ϕ_{ε} changes from 0 to 1, representing the diffuse cell boundary. The region $\Omega_{\varepsilon}^+(t)$ is the cell region at t. Note that, by the imposed boundary conditions $u_{\varepsilon} = 0$ on $\partial\Omega$, the boundary $\partial\Omega$ is included in the closure of $\Omega_{\varepsilon}^-(t)$. We further assume that the inner region $I_{\varepsilon}(t)$ is an $O(\varepsilon)$ -neighborhood of a closed and smooth surface $\Gamma(t)$, independent of ε , that is the limit of $\{x \in \Omega : \phi_{\varepsilon}(x,t) = 1/2\}$ as $\varepsilon \to 0$. Moreover, the interior and exterior of $\Gamma(t)$, denoted $\Omega^+(t)$ and $\Omega^-(t)$, are the limit as $\varepsilon \to 0$ of $\Omega_{\varepsilon}^+(t)$ and $\Omega_{\varepsilon}^-(t)$, respectively, with $\Omega^+(t)$ being the cell region. We note that the terms inner region and outer region are defined with respect to an interface. They are commonly used in matched asymptotic analysis for the passage of a phase-field model to its sharp-interface limit; cf. [39] and the references therein.

Outer expansions. We assume the following expansions in the outer region $O_{\varepsilon}(t)$:

$$\phi_{\varepsilon}(x,t) = \phi_0(x,t) + \varepsilon\phi_1(x,t) + \varepsilon^2\phi_2(x,t) + \cdots,$$

$$u_{\varepsilon}(x,t) = u_0(x,t) + \varepsilon u_1(x,t) + \varepsilon^2 u_2(x,t) + \cdots,$$

$$v_{\varepsilon}(x,t) = v_0(x,t) + \varepsilon v_1(x,t) + \varepsilon^2 v_2(x,t) + \cdots,$$

where the functions $\phi_i(x,t)$, $u_i(x,t)$, and $v_i(x,t)$ (i=0,1,...) are smooth and bounded, and are independent of ε . They also satisfy the boundary conditions $\phi_i = u_i = v_i = 0$ on $\partial\Omega$. Note that these functions are different from those in the expansions with a different time scale τ . Since $\phi_0 = O(\varepsilon^2)$ in $\Omega_{\varepsilon}^-(t)$, there will be no equations for u_{ε} and v_{ε} at leading order O(1), we shall assume that $u_{\varepsilon} = 0$ and $v_{\varepsilon} = 0$ in $\Omega_{\varepsilon}^-(t)$. If we plug the above expansion of ϕ_{ε} , u_{ε} , and v_{ε} into (2.1), (2.2), and (2.3), we obtain that, up to the leading order O(1),

$$\partial_t u_0 = D_1 \Delta u_0 + f(u_0, v_0) \quad \text{in } \Omega^+(t) \times (0, \infty),$$
 (2.5)

$$\partial_t v_0 = D_2 \Delta v_0 + g(u_0, v_0) \quad \text{in } \Omega^+(t) \times (0, \infty).$$
 (2.6)

Local coordinates for the inner region. Let $x \in I_{\varepsilon}(t)$ and denote by s(x,t) the signed distance from x to $\Gamma(t)$, with s(x,t) > 0 if x is inside $\Gamma(t)$ and s(x,t) < 0 otherwise. Note that $s(x,t) = O(\varepsilon)$ and $|\nabla s(x,t)| = 1$. Now, let $y = P(x,t) \in \Gamma(t)$ be the projection of x onto $\Gamma(t)$, defined by |x-P(x,t)| = |s(x,t)|. (We use $|\cdot|$ to denote both the absolute value of a number and the Euclidean norm of a vector.) For $0 < \varepsilon \ll 1$, the projection $y = P(x,t) \in \Gamma(t)$ is unique, and the vector x - P(x,t) is normal to the surface $\Gamma(t)$ at y = P(x,t). Let $z = s(x,t)/\varepsilon$. Let $n = n(y,t) = \nabla s(y,t)$ be the unit normal at $y \in \Gamma(t)$ pointing from the exterior to the interior of $\Gamma(t)$. Then we have a unique expression of $x \in I_{\varepsilon}(t)$ as

$$x = y + \varepsilon z n. \tag{2.7}$$

We call (y, z) the local coordinate of $x \in I_{\varepsilon}(t)$ with respect to the surface $\Gamma(t)$. We have for $0 < \varepsilon \ll 1$ that [16, 18, 26, 39, 42]

$$\nabla_x z = \varepsilon^{-1} n(y, t) + O(1), \tag{2.8}$$

$$\Delta_x z = 2\varepsilon^{-1} H(y, t) + O(1), \tag{2.9}$$

$$\partial_t z = -\varepsilon^{-1} V(y, t), \tag{2.10}$$

$$\nabla_x y_j(x,t) \cdot n(y,t) = 0 \quad (j = 1, 2, 3), \tag{2.11}$$

where H(y,t) is the mean curvature of the surface $\Gamma(t)$ at the point y=P(x,t), V(y,t) is the normal velocity of the point $y=P(x,t)\in\Gamma(t)$ defined by

$$V(y,t) = \partial_t y \cdot n(y,t) = \partial_t P(x,t) \cdot n(y,t), \tag{2.12}$$

and y_j (j=1,2,3) are the components of y=y(x,t). Let f=f(x,t) and $\tilde{f}=\tilde{f}(z,y,t)$ be smooth functions such that $f(x,t)=\tilde{f}(z,y,t)$ with $x\in I_{\varepsilon}(t)$ and (y,z) related by (2.7). Then, by (2.8)–(2.12) and the chain rule, we obtain for $0<\varepsilon\ll 1$ that [16,18,26,39,42]

$$\nabla_x f(x,t) = \varepsilon^{-1} n \,\partial_z \tilde{f}(y,z,t) + O(1), \tag{2.13}$$

$$\Delta_x f(x,t) = \left(\varepsilon^{-1} 2H(y,t)\partial_z + \varepsilon^{-2} \partial_{zz}^2\right) \tilde{f}(y,z,t) + O(1), \tag{2.14}$$

$$\partial_t f(x,t) = -\varepsilon^{-1} V(y,t) \,\partial_z \tilde{f}(y,z,t) + O(1). \tag{2.15}$$

Inner expansions. We now assume the following expansions in the inner region $I_{\varepsilon}(t)$:

$$\phi_{\varepsilon}(x,t) = \tilde{\phi}_{0}(y,z,t) + \varepsilon \tilde{\phi}_{1}(y,z,t) + \varepsilon^{2} \tilde{\phi}_{2}(y,z,t) + \cdots,$$

$$u_{\varepsilon}(x,t) = \tilde{u}_{0}(y,z,t) + \varepsilon \tilde{u}_{1}(y,z,t) + \varepsilon^{2} \tilde{u}_{2}(y,z,t) + \cdots,$$

$$v_{\varepsilon}(x,t) = \tilde{v}_{0}(y,z,t) + \varepsilon \tilde{v}_{1}(y,z,t) + \varepsilon^{2} \tilde{v}_{2}(y,z,t) + \cdots,$$

where $x \in I_{\varepsilon}(t)$ and (y,z) are related by (2.7), and all $\tilde{\phi}_i = \tilde{\phi}_i(y,z,t)$, $\tilde{u}_i = \tilde{u}_i(y,z,t)$, and $\tilde{v}_i = \tilde{v}_i(y,z,t)$ ($i=0,1,\ldots$) are smooth and bounded functions. Let us substitute ϕ_{ε} , u_{ε} , and v_{ε} in (2.1)–(2.3) with these expansions. By (2.13)–(2.15) and a series of calculations, we obtain

$$-\varepsilon^{-1}V\partial_z\tilde{\phi}_0 = \varepsilon^{-1}h(u_0, v_0) \left| \partial_z\tilde{\phi}_0 \right| + \varepsilon^{-2}\gamma \left[\partial_{zz}\tilde{\phi}_0 - W'(\tilde{\phi}_0) \right]$$
$$+ \varepsilon^{-1}\gamma \left[2H\partial_z\tilde{\phi}_0 + \partial_{zz}\tilde{\phi}_1 - W''(\tilde{\phi}_0)\tilde{\phi}_1 \right] + O(1),$$

where V=V(y,t) and H=H(y,t) are the normal velocity and mean curvature, respectively, at y=P(x,t). Note that, unlike ϕ_{ε} which varies from 0 to 1, the concentration fields u_{ε} and v_{ε} should not vary largely, in the inner region. In particular, we have $\tilde{u}_0(y,z,t)=\tilde{u}_0(y,0,t)+O(\varepsilon)$ and $\tilde{v}_0(y,z,t)=\tilde{v}_0(y,0,t)+O(\varepsilon)$, as $|x-y|=|x-P(x,t)|=O(\varepsilon)$ for any $x\in I_{\varepsilon}(t)$ with the local coordinate (y,z). Therefore, we obtain from the above equation that

$$-\varepsilon^{-1}V\partial_z\tilde{\phi}_0 = \varepsilon^{-1}h(\tilde{u}_0(y,0,t),\tilde{v}_0(y,0,t))\left|\partial_z\tilde{\phi}_0\right| + \varepsilon^{-2}\gamma\left[\partial_{zz}\tilde{\phi}_0 - W'(\tilde{\phi}_0)\right] + \varepsilon^{-1}\gamma\left[2H\partial_z\tilde{\phi}_0 + \partial_{zz}\tilde{\phi}_1 - W''(\tilde{\phi}_0)\tilde{\phi}_1\right] + O(1).$$

Now, equating the terms with the same order $O(\varepsilon^{-2})$ and $O(\varepsilon^{-1})$, respectively, we get

$$O(\varepsilon^{-2}): \qquad 0 = \partial_{zz}\tilde{\phi}_0 - W'(\tilde{\phi}_0), \tag{2.16}$$

$$O(\varepsilon^{-1}): \qquad -V\partial_z\tilde{\phi}_0 = h(\tilde{u}_0(y,0,t),\tilde{v}_0(y,0,t)) \left| \partial_z\tilde{\phi}_0 \right| + \gamma \left[2H\partial_z\tilde{\phi}_0 + \partial_{zz}\tilde{\phi}_1 - W''(\tilde{\phi}_0)\tilde{\phi}_1 \right]. \tag{2.17}$$

Similarly, we can plug the inner expansions of ϕ_{ε} , u_{ε} , and v_{ε} into (2.2) and (2.3) to get in the leading order that

$$O\left(\varepsilon^{-2}\right): \qquad 0 = D_1\left(\partial_z\tilde{\phi}_0\partial_z\tilde{u}_0 + \tilde{\phi}_0\partial_{zz}\tilde{u}_0\right),$$
 (2.18)

$$O\left(\varepsilon^{-2}\right): \qquad 0 = D_2\left(\partial_z \tilde{\phi}_0 \partial_z \tilde{v}_0 + \tilde{\phi}_0 \partial_{zz} \tilde{v}_0\right).$$
 (2.19)

Inner-outer matching and the sharp-interface limit. Since in the outer region $\phi_{\varepsilon} = O(\varepsilon^2)$ in $\Omega_{\varepsilon}^-(t)$ and $\phi_{\varepsilon} = 1 + O(\varepsilon^2)$ in $\Omega_{\varepsilon}^+(t)$, we have the following matching conditions for the leading-order terms of the inner and outer solutions of the phase field ϕ_{ε} :

$$\lim_{z \to -\infty} \tilde{\phi}_0(y, z, t) = 0 \quad \text{and} \quad \lim_{z \to \infty} \tilde{\phi}_0(y, z, t) = 1. \tag{2.20}$$

These, together with (2.16), determine completely $\tilde{\phi}_0$ to be

$$\tilde{\phi}_0(y, z, t) = \frac{1}{2} + \frac{e^{3z} - e^{-3z}}{2(e^{3z} + e^{-3z})} \quad \forall z \in \mathbb{R}.$$

In particular, $\tilde{\phi}_0$ does not depend on y and t. One can verify that $\partial_z \tilde{\phi}_0 > 0$ and that

$$\int_{-\infty}^{\infty} (\partial_z \tilde{\phi}_0)^2 dz = 1. \tag{2.21}$$

By matching the inner expansion and outer expansion, we have $\partial_z \tilde{\phi}_0(\pm \infty) = \partial_{zz} \tilde{\phi}_0(\pm \infty) = 0$. Thus, by integration by parts and (2.16), we have

$$\int_{-\infty}^{\infty} \partial_z \tilde{\phi}_0 \left[\partial_{zz} \tilde{\phi}_1 - W''(\tilde{\phi}_0) \tilde{\phi}_1 \right] dz = \int_{-\infty}^{\infty} \partial_z \left[\partial_{zz} \tilde{\phi}_0 - W'(\tilde{\phi}_0) \right] \tilde{\phi}_1 dz = 0.$$
 (2.22)

Now, by multiplying both sides of (2.17) by $\partial_z \tilde{\phi}_0$ and then integrating the resulting equation over $z \in (-\infty, \infty)$, we have by (2.21) and (2.22) that

$$V(y,t) = -h(u_0(y,0,t), v_0(y,0,t)) - 2\gamma H(y,t) \qquad \forall y \in \Gamma(t).$$
(2.23)

It follows from (2.18) and (2.19) that $\partial_z(\tilde{\phi}_0\partial_z\tilde{u}_0) = \partial_z\tilde{\phi}_0\partial_z\tilde{u}_0 + \tilde{\phi}_0\partial_{zz}\tilde{u}_0 = 0$ and similarly $\partial_z(\tilde{\phi}_0\partial_z\tilde{v}_0) = 0$ for all $z \in \mathbb{R}$. These and the matching conditions (2.20) imply that

$$0 = \lim_{z \to -\infty} \tilde{\phi}_0(y, z, t) \partial_z \tilde{u}_0(y, z, t) = \lim_{z \to \infty} \tilde{\phi}_0(y, z, t) \partial_z \tilde{u}_0(y, z, t) = \lim_{z \to \infty} \partial_z \tilde{u}_0(y, z, t),$$

$$0 = \lim_{z \to -\infty} \tilde{\phi}_0(y, z, t) \partial_z \tilde{v}_0(y, z, t) = \lim_{z \to \infty} \tilde{\phi}_0(y, z, t) \partial_z \tilde{v}_0(y, z, t) = \lim_{z \to \infty} \partial_z \tilde{v}_0(y, z, t).$$

Matching the inner expansions and outer expansions, we thus have

$$\partial_n u_0(x,t) = \lim_{z \to \infty} \partial_z \tilde{u}_0(y,z,t) = 0 \qquad \forall x \in \Gamma(t),$$
 (2.24)

$$\partial_n v_0(x,t) = \lim_{z \to \infty} \partial_z \tilde{u}_0(y,z,t) = 0 \qquad \forall x \in \Gamma(t), \tag{2.25}$$

where u_0 and v_0 are the leading-order terms in the outer expansion of u_{ε} and v_{ε} , and satisfy (2.5) and (2.6), respectively.

We summarize our analysis in the following:

Theorem 2.1. Under the assumption that there exists a closed and smooth interface $\Gamma(t)$, the outer and inner expansions above for the solutions ϕ_{ε} , u_{ε} , and v_{ε} are valid, and the corresponding matching conditions are satisfied, the following hold true in the limit $\varepsilon \to 0$:

- (1) The phase-field function ϕ_{ε} converges to 1 in $\Omega^+(t)$ and 0 in $\Omega^-(t)$, respectively;
- (2) The concentrations u_{ε} and v_{ε} converge to the solution to the boundary-value problem of the reaction-diffusion equations (2.5) and (2.6), and (2.24) and (2.25);
- (3) The normal velocity V = V(x,t) of the sharp cell boundary $\Gamma(t)$ is given by (2.23).

3 Numerical Methods

We describe our numerical methods for solving the system of equations (1.1)–(1.4) in the twodimensional setting in the following non-dimensionalized form for the rescaled normal velocity V = V(x, y, t) on the rescaled cell boundary $\Gamma(t)$ at time t, rescaled concentrations u = u(x, y, t) and v = v(x, y, t) defined on the cell region $\Omega^+(t)$, respectively:

$$V = u - u^* - \chi H \qquad \text{for } (x, y) \in \Gamma(t) \text{ and } t > 0, \tag{3.1}$$

$$\partial_t u = D_u \Delta u + f(u, v)$$
 for $(x, y) \in \Omega^+(t)$ and $t > 0$, (3.2)

$$\partial_t v = D_v \Delta v - f(u, v) \quad \text{for } (x, y) \in \Omega^+(t) \text{ and } t > 0,$$
 (3.3)

$$\partial_n u = \partial_n v = 0$$
 for $(x, y) \in \Gamma(t)$ and $t > 0$, (3.4)

where H is the rescaled curvature, all u^* , χ , D_u , D_v , K, and C are positive constants, and

$$f(u, v) = -Ku(u - 0.5)(u - Cv).$$

Details of the non-dimensionalization are given in section 4.1 below. Our numerical methods for the one-species system, which is the sharp-interface limit of the system (1.7)–(1.9), are similar.

We set our computational box to be $\Omega=(-L,L)^2$ for some L>0 and cover it with a uniform finite-difference grid with step size h in each dimension. We discretize a time interval [0,T] with T>0 the final time of interest by $t_m=m\Delta t$ $(m=0,1,\ldots)$ with time step $\Delta t>0$. We denote by Γ_m , Ω_m^+ , and Ω_m^- the approximation of $\Gamma(t_m)$, $\Omega^+(t_m)$, and $\Omega^-(t_m)$, respectively, where $\Omega^-(t)=\Omega\backslash\Omega^+(t)$ (an overline denotes the closure). For a function w=w(x,y,t) with $(x,y)\in\Omega$ and $t\geq 0$, we denote by $w^m=w^m(x,y)$ the approximation of $w(x,y,t_m)$, and by $w_{i,j}^m$ the approximation of $w^m(x_i,y_j)$ for a grid point (x_i,y_j) or the center (x_i,y_j) of a grid cell. Note that we approximate the level-set function ϕ at grid points while we approximate the concentrations u and v at the centers of grid cells; see below.

The Level-set method for the moving cell boundary. We capture the cell boundary $\Gamma(t)$ at time t by using the level-set method [35, 36], with level-set function $\phi = \phi(x, y, t)$, i.e., $\Gamma(t) = \{(x,y) \in \Omega : \phi(x,y,t) = 0\}$. The level-set function is determined by the evolution equation $\partial_t \phi + V |\nabla \phi| = 0$, where V = V(x,y,t) is given in (3.1) that needs to be extended from $\Gamma(t)$ to the entire computational domain Ω . The first part of our normal velocity is $u(x,y,t) - u^*$. We keep the value of u = u(x,y,t) in $\Omega^+(t)$ and additionally extend it from $\Gamma(t)$ to $\Omega^-(t)$ numerically in each step of time iteration. Note, for convenience, we continue to denote the result by u = u(x,y,t), now for $(x,y) \in \Omega$. (Details of such extension are given below.) The curvature H can be extended simply by using $H = \nabla \cdot (\nabla \phi/|\nabla \phi|)$ for all $(x,y) \in \Omega$. Note that implicitly we require that the level-set function to be close to the signed distance to the interface $\Gamma(t)$ with $\phi < 0$ in $\Omega^+(t)$ (the cell region) and $\phi > 0$ in $\Omega^-(t)$, at least near $\Gamma(t)$. Therefore, the level-set equation and boundary conditions become now

$$\partial_t \phi = -(u - u^*)|\nabla \phi| + \chi \left(\nabla \cdot \frac{\nabla \phi}{|\nabla \phi|}\right)|\nabla \phi| \qquad \text{for } (x, y) \in \Omega \text{ and } t > 0,$$
(3.5)

$$\partial_n \phi = 0$$
 for $(x, y) \in \partial \Omega$ and $t > 0$. (3.6)

Following [46], we rewrite the curvature part of the normal velocity as

$$\nabla \cdot \left(\frac{\nabla \phi}{|\nabla \phi|}\right) |\nabla \phi| = \Delta \phi - N(\phi),$$

$$N(\phi) = \frac{\nabla \phi}{|\nabla \phi|} \cdot \nabla(|\nabla \phi|) = \frac{\phi_x^2 \phi_{xx} + 2\phi_x \phi_y \phi_{xy} + \phi_y^2 \phi_{yy}}{\phi_x^2 + \phi_y^2}.$$

With a given initial level-set function $\phi(x, y, 0)$ for all $(x, y) \in \Omega$, we can solve (3.5) and (3.6) numerically with finite difference schemes in time and over the uniform grid.

Specifically, starting from $u_{i,j}^m$ at centers of grid cells, we first use polynomial interpolation or extrapolation to approximate u at points where the interface intersects grid lines. Such intersection points are located by the linear interpolation of the values of ϕ at grid points. We then extend these approximate u-values from the points on the interface to all the grid points in the outer region Ω_m^+ , constant in the normal direction, by the fast sweeping method [51,53]. We continue to denote the extended function by u^m . To get ϕ^{m+1} , we then use the semi-implicit scheme

$$\frac{\phi^{m+1} - \phi^m}{\Delta t} = -(u^m - u^*)|\nabla\phi^m| + \chi\Delta\phi^{m+1} - \chi N_{\epsilon}(\phi^m), \tag{3.7}$$

where $N_{\epsilon}(\phi)$ is the same as $N(\phi)$ except the denominator $\phi_x^2 + \phi_y^2$ in $N(\phi)$ is replaced by $\phi_x^2 + \phi_y^2 + \epsilon$ in $N_{\epsilon}(\phi)$ for a small enough $\epsilon > 0$, to avoid singularities at $\nabla \phi = 0$ while keeping an accurate approximation away from them. We use $\epsilon = 10^{-12}$ in all of our simulations. We discretize $|\nabla \phi^m|$ by fifth-order WENO [20] within Godunov's scheme [37], and discretize $\Delta \phi$ and $N_{\epsilon}(\phi)$ by second-order central differencing.

At the boundary of the computational domain Ω , we use a second-order scheme to discretize the Neumann boundary conditions (3.6). The coefficient matrix of the resulting system of linear equations for all $\phi_{i,j}^{m+1}$ is sparse and nonsymmetric, with the nonsymmetry due mainly to the chosen treatment of the boundary conditions. We solve the linear system of equations using the biconjugate gradient stabilized method preconditioned with the incomplete LU decomposition. Finally, we reinitialize the level-set function ϕ^{m+1} , performing a few iterations of the algorithm of redistancing to signed distance function [49], and continue to denote the result by ϕ^{m+1} .

Discretization of the reaction-diffusion equations on a moving cell region. Given Γ_{m+1} , Ω_{m+1}^+ , and Ω_{m+1}^- , all specified by the level-set function ϕ^{m+1} on all the grid points, and also given the concentrations u^m and v^m on all the centers in Ω_m^+ of grid cells, we need to find the approximate solution u^{m+1} and v^{m+1} on all the centers of grid cells that overlap with Ω_{m+1}^+ by the equations and boundary conditions (3.2)–(3.4). To do so, we first employ a second-order extrapolation method proposed in [22] to extend u^m and v^m to the centers of grid cells that overlap with the new cell region Ω_{m+1}^+ but are not in Ω_m^+ ; cf. black solid dotes in Figure 3.1. We denote by $\tilde{u}_{i,j}^m$ and $\tilde{v}_{i,j}^m$ the extended u-value and v-value, or the original values u^m and v^m if they are not extended, at the center of a grid cell in Ω_{m+1}^+ labelled by (i,j). Note by (3.2)–(3.4) that the integral of u+v over Ω is a constant with respect to time t (cf. (1.6)), and its value is determined by the initial concentrations u and v at t=0. We shall still denote this constant by M. To enforce this conservation of the total mass, we modify the value $\tilde{v}_{i,j}^m$ to get $v_{i,j}^m$ at centers of all the grid cells overlapping with Ω_{m+1}^+ by

$$v_{i,j}^{m} = \frac{1}{\text{Area}(\Omega_{m+1}^{+})} \left[M - \int_{\Omega_{m+1}^{+}} (\tilde{u}^{m} + \tilde{v}^{m}) dA \right] + \tilde{v}_{i,j}^{m}.$$

Note that we only correct the v-values as v is the fast diffusion component. The finally extended u and v values are now denoted by $u_{i,j}^m$ and $v_{i,j}^m$; they are defined on centers labelled by (i,j) of grid cells overlapping with Ω_{m+1}^+ .

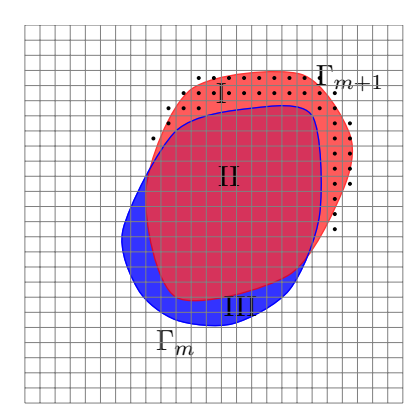


Figure 3.1: Illustration of two consecutive cell regions Ω_m^+ and Ω_{m+1}^+ . The cell region Ω_m^+ is the union of part II and part III, enclosed by the cell boundary Γ_m (blue curve). The cell region Ω_{m+1}^+ is the union of part I and part II, marked by red. Black solid dots mark those centers of grid cells that are in Ω_{m+1}^+ but not in Ω_m^+ .

We now focus on u^{m+1} as v^{m+1} is similar. We use the semi-implicit scheme

$$\frac{u^{m+1} - u^m}{\Delta t} = D_u \Delta u^{m+1} + f(u^m, v^m) \quad \text{for } (x, y) \in \Omega_{m+1}^+.$$

Since the interface Γ_{m+1} cuts through grid cells, we employ an embedded boundary method developed in [38] to discretize the Laplacian operator. Fix a grid cell $C_{i,j}$ that overlaps with Ω_{m+1}^+ and that is centered at (x_i, y_j) . Integrating both sides of the above equation over $C_{i,j} \cap \Omega_{m+1}^+$, we have by the divergence theorem that

$$\int_{\mathcal{C}_{i,j} \cap \Omega_{m+1}^+} \frac{u^{m+1} - u^m}{\Delta t} dA = D_u \int_{\partial(\mathcal{C}_{i,j} \cap \Omega_{m+1}^+)} \nabla u^{m+1} \cdot \nu \, dl + \int_{\mathcal{C}_{i,j} \cap \Omega_{m+1}^+} f(u^m, v^m) \, dA, \qquad (3.8)$$

where ν is the unit vector normal to the boundary $\partial(\mathcal{C}_{i,j} \cap \Omega_{m+1}^+)$. The two area integrals can be approximated by

$$\int_{\mathcal{C}_{i,j}\cap\Omega_{m+1}^{+}} \frac{u^{m+1} - u^{m}}{\Delta t} dA \approx \frac{u_{i,j}^{m+1} - u_{i,j}^{m}}{\Delta t} \operatorname{Area}\left(\mathcal{C}_{i,j}\cap\Omega_{m+1}^{+}\right), \tag{3.9}$$

$$\int_{\mathcal{C}_{i,j}\cap\Omega_{m+1}^+} f(u^m, v^m) dA \approx f(u_{i,j}^m, v_{i,j}^m) \operatorname{Area} (\mathcal{C}_{i,j}\cap\Omega_{m+1}^+).$$
(3.10)

The area can be calculated using the level-set function ϕ^{m+1} [28]. Whether or not the interface Γ_{m+1} cuts through the grid cell $C_{i,j}$, by the boundary condition $\partial_n u^{m+1} = 0$ on Γ_{m+1} , we can approximate the line integral in (3.8) by [38]

$$\int_{\partial(\mathcal{C}_{i,j}\cap\Omega_{m+1}^{+})} \nabla u^{m+1} \cdot \nu \, dl \approx \frac{u_{i+1,j}^{m+1} - u_{i,j}^{m+1}}{h} L_{i+1/2,j} - \frac{u_{i,j}^{m+1} - u_{i-1,j}^{m+1}}{h} L_{i-1/2,j} + \frac{u_{i,j+1}^{m+1} - u_{i,j}^{m+1}}{h} L_{i,j+1/2} - \frac{u_{i,j}^{m+1} - u_{i,j-1}^{m+1}}{h} L_{i,j-1/2}, \tag{3.11}$$

where $L_{i\pm 1/2,j} \in [0,h]$ and $L_{i,j\pm 1/2} \in [0,h]$ refer to the length of the corresponding edge of the grid cell $C_{i,j}$ inside Ω_{m+1}^+ . These lengths can be calculated using the level-set function ϕ^{m+1} that defines the interface Γ_{m+1} [28].

The coefficient matrix of the resulting system of linear equations is symmetric positive definite [38], and the system can be solved by the conjugate gradient method with an incomplete Cholesky preconditioner or by an algebraic multigrid method.

Algorithm.

- Step 0. Input all the parameters. Set the computational box $\Omega = (-L, L)^2 \subset \mathbb{R}^2$ and cover it with a uniform finite-difference grid with grid size h. Discretize the time interval [0, T] of interest with time step Δt . Initialize the level-set function ϕ^0 and the concentrations u^0 and v^0 . Set m = 0.
- Step 1. Extend the normal velocity from the interface to the entire computational box. Solve the semi-implicit discretization equation (3.7) to get the updated level-set function ϕ^{m+1} . Reinitialize the level-set function and still denote it by ϕ^{m+1} .
- Step 2. Extend u^m and v^m to centers of grid cells overlapping with Ω_{m+1}^+ defined by ϕ^{m+1} . Solving the semi-implicit discretization equations (cf. (3.8)–(3.11)) to obtain u^{m+1} and v^{m+1} .
- Step 3. Check if the cell region Ω_{m+1}^+ touches the boundary $\partial\Omega$. If so, shift the computational box so that the cell is centered in the new computational box, still denoted Ω .
- Step 4. Set m := m + 1. Repeat Steps 1–3 until the final simulation time is reached.

Convergence test. We have tested our numerical methods and code. In Figure 3.2, we show that the total mass conservation is captured numerically in a long time simulation. We have also used our numerical methods to simulate a moving cell with the final (rescaled) time being T=10, using different time steps and different spatial grid sizes. Figure 3.3 shows our simulation results. They indicate that our numerical method and algorithm converge both in time and space.

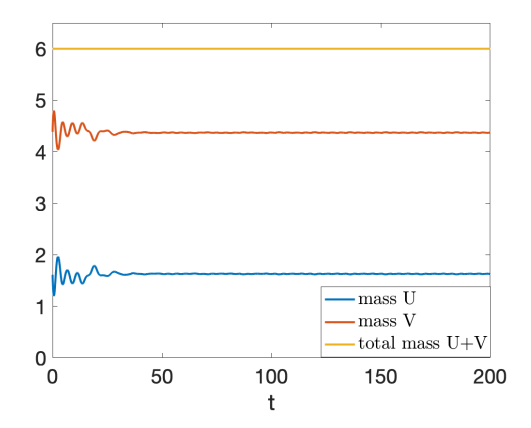


Figure 3.2: Numerical conservation of total mass. Here U = U(t) and V = V(t) at time t are defined as the integral of u(x, y, t) and v(x, y, t), respectively, over the cell region $\Omega^+(t)$, and the total mass is defined to be the sum U + V.

To further test the convergence rate of our method, we solve numerically the following moving boundary problem:

$$\begin{cases} \partial_t u = \Delta u - u - 4 + x^2 + y^2 & \text{in } \Omega^+(t), \\ \partial_n u = 2\sqrt{x^2 + y^2} & \text{on } \Gamma(t) = \partial(\Omega^+(t)), \\ V = -H + \sqrt{u} & \text{on } \Gamma(t), \end{cases}$$

where $\Gamma(t)$ is the moving boundary, $\Omega^+(t)$ is the interior region of $\Gamma(t)$, V is the normal velocity on $\Gamma(t)$, H is the curvature of $\Gamma(t)$, and u = u(x, y, t) with $(x, y) \in \Omega^+(t)$. This system has a radially symmetric solution: the boundary $\Gamma(t)$ is a circle of radius R(t) and $u(x, y, t) = \tilde{u}(r, t)$ with

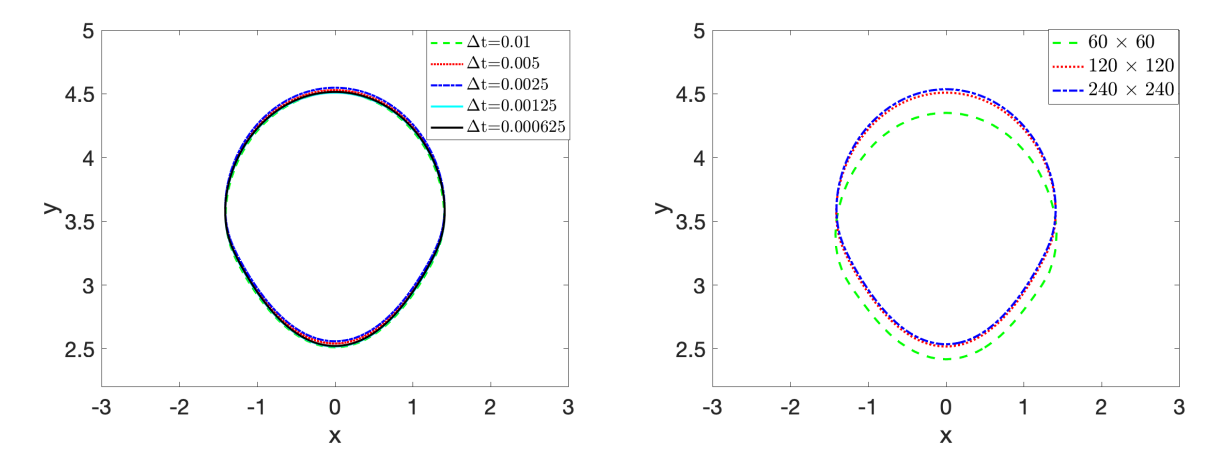


Figure 3.3: Simulated cell shapes with the final simulation time T=10. The initial simulation box $\Omega=(-3,3)^2$ is shifted during the simulation. Left: Simulation results with the grid size h=0.05 and different time steps Δt . Right: Simulation results with the time step $\Delta t=1.25\times 10^{-3}$ and with different number of grid points.

 $r = \sqrt{x^2 + y^2}$, given by (dropping the tilde)

$$\begin{cases} u(r,t) = r^2 & \text{for } r < R(t), \\ R(t) = \sqrt{1 + (R_0^2 - 1)e^{-2t}} & \text{for } t > 0. \end{cases}$$

For our level-set numerical simulations, the initial boundary is set to be a circle of radius $R_0 = 1.3$ centered at the origin. To show the error between the simulated and exact boundary location at a final time T of simulation, we locate numerically a set of intersection points $\{P_1, \dots, P_N\}$ of the numerical level-set $\phi_{\rm appr} = 0$ at T and the grid lines using linear interpolation [29], where $\phi_{\rm appr}$ denotes our numerical level-set function at T. We also denote by $\phi_{\rm exact}$ the signed distance function of the boundary $\Gamma(T)$ which is the circle of radius R(T), and further define

$$\phi_{\text{err}}^{1} = \frac{1}{N} \sum_{i=1}^{N} |\phi_{\text{exact}}(P_i) - \phi_{\text{appr}}(P_i)| = \frac{1}{N} \sum_{i=1}^{N} |\phi_{\text{exact}}(P_i)|,$$

$$\phi_{\text{err}}^{\infty} = \max_{1 \le i \le N} |\phi_{\text{exact}}(P_i) - \phi_{\text{appr}}(P_i)| = \max_{1 \le i \le N} |\phi_{\text{exact}}(P_i)|.$$

In Table 1, we compare our numerical and exact solutions at the final time T=0.4 with varying grid sizes and time steps for the approximation of the concentration u inside the simulated boundary defined by $\phi_{\rm appr}=0$. In the table, $u_{\rm appr}$ and $u_{\rm exact}$ denote the numerical and exact solutions, respectively, and $\|\cdot\|_2$ and $\|\cdot\|_\infty$ denote the L^2 and L^∞ norms, respectively. In Table 2, we compare our numerical and exact solutions at the final time T=0.4 with varying grid sizes and time steps for the approximation of the boundary. In both tables, h and Δt are the grid size of a uniform spatial grid and the step size of time discretization, respectively. We observe that the convergence rate for the approximation of u is of the second order in both space and time, better than the expected second-order in space and first-order in time. Similarly, our numerical approximation of the boundary location is between the first and the second order in both space and time, again better than the expected first-order in space. These better convergence results are due to the fact that in our test problem u=u(r,t) is independent of t.

Table 1: Numerical accuracy for u.

h	Δt	$ u_{\text{appr}} - u_{\text{exact}} _2$	Order	$ u_{\mathrm{appr}} - u_{\mathrm{exact}} _{\infty}$	Order
0.15	0.15	1.600×10^{-3}	-	2.200×10^{-3}	-
7.500×10^{-2}	7.500×10^{-2}	3.190×10^{-4}	2.33	5.135×10^{-4}	2.10
3.750×10^{-2}	3.750×10^{-2}	1.435×10^{-4}	1.15	1.640×10^{-4}	1.64
1.875×10^{-2}	1.875×10^{-2}	3.295×10^{-5}	2.12	3.944×10^{-5}	2.06
9.375×10^{-3}	9.375×10^{-3}	6.85×10^{-6}	2.27	8.943×10^{-6}	2.14

Table 2: Numerical accuracy for the boundary.

h	Δt	$\phi_{ m err}^1$	Order	$\phi_{ m err}^{\infty}$	Order	
0.15	0.15	9.030×10^{-2}	-	1.073×10^{-1}	-	
7.500×10^{-2}	7.500×10^{-2}	2.970×10^{-2}	1.60	3.540×10^{-2}	1.60	
3.750×10^{-2}	3.750×10^{-2}	8.600×10^{-3}	1.79	1.040×10^{-2}	1.77	
1.875×10^{-2}	1.875×10^{-2}	2.500×10^{-3}	1.78	3.100×10^{-3}	1.75	
9.375×10^{-3}	9.375×10^{-3}	1.100×10^{-3}	1.18	1.500×10^{-3}	1.05	

4 Simulation Results and Analysis

We perform numerical simulations to study the cell polarization in response to various external stimulus and the trajectory of a moving cell, and analyze these simulation results in terms of the modeling and parameters.

4.1 Parameters and Non-dimensionalization

In Table 3, we collect all the parameters in the original model (1.1)–(1.4), and describe their meanings and units. We also provide their estimated values following [11,44]. To non-dimensionalize our equations (1.1)–(1.4), we follow [11] to introduce two parameters. One is the typical cell speed V_0 which is in the range $\sim 0.1 \,\mu\text{m/s}$. The other is the typical radius of a cell R which is in the range $\sim 10 \,\mu\text{m}$. We then introduce non-dimensionalized parameters according to Table 4. We then define $\hat{x} = x/R$, $\hat{t} = (V_0/R)t$, $\hat{u} = u/c$, $\hat{v} = v/c$, and $\hat{V} = V/V_0$, and convert the original system of equations (1.1)–(1.4) into the non-dimensionalized system of equations for \hat{V} , \hat{u} , and \hat{v} , which is, after dropping all the hat, the system (3.1)–(3.4).

4.2 Cell Polarization

Inspired by the one-dimensional simulations of the wave-pinning mechanism [33], we consider a non-moving or stationary cell that occupies the fixed region Ω^+ whose boundary is the curve

$$x = (1 - 0.3\cos 2\theta)\cos \theta, \quad y = (1 - 0.3\cos 2\theta)\sin \theta \qquad \forall \theta \in [0, 2\pi).$$

We set K = 500, M = 6, C = 0.8, $D_u = 0.3$, and $D_v = 30$. (Note that χ and μ^* are not needed, since the boundary is fixed.) The computational box is $\Omega = (-2.5, 2.5) \times (-2.5, 2.5)$. Note that $\Omega^+ \subset \Omega$. We cover Ω by a uniform finite-difference grid of grid size h = 0.05 and set $\Delta t = 0.001$.

Random initial value. We choose the initial value u_0 to be a random variable defined on all the grid centers. The values are generated uniformly at random from [0, 0.8]. We also set the initial value

Table 3: Model Parameters

Parameters	Description	Estimated Values	Units
D_u	diffusion coefficient of u	$0.1 \sim 0.5$	$\mu \mathrm{m}^2/\mathrm{s}$
D_v	diffusion coefficient of v	$10 \sim 50$	$\mu\mathrm{m}^2/\mathrm{s}$
α	coefficient of F-actin extension	0.1	$\mathrm{pN}/\mu\mathrm{m}$
β	coefficient for myosin retraction	0.2	$\mathrm{pN}/\mu\mathrm{m}$
au	friction coefficient	2.62	$\mathrm{pNs}/\mathrm{\mu m}^2$
γ	surface tension	1	pN
k	relative reaction rate	~ 0.01	s^{-1}
c	concentration of u at the cell front	$1 \sim 10$	concentration unit
C	interconversion parameter	$0.5 \sim 0.8$	unitless

Table 4: Nondimensionalized Parameters

Parameters	Description	Estimated Values
$\widehat{D}_u = \frac{D_u}{V_0 R}$	Rescaled diffusive coefficient of u	$0.1 \sim 0.5$
$\widehat{D}_v = \frac{\widetilde{D_v}}{V_0 R}$	Rescaled diffusive coefficient of v	$10 \sim 50$
$K = \frac{kRc^2}{V_0}$	Rescaled reaction rate compared to motility	$100\sim 500$
$\chi = \frac{\gamma}{V_0 \tau R}$	Relative strength of surface tension	$0.1 \sim 0.3$
$ \chi = \frac{\gamma}{V_0 \tau R} \widehat{u^*} = \frac{\beta}{c\alpha} $	Rescaled contractility	$0.2\sim0.45$
$\widehat{M} = \frac{N_{tot}}{\mathrm{cR}^2}$	Rescaled total amount of protein u and v	$6 \sim 8$
C	interconversion parameter	$0.5 \sim 0.8$

 v_0 to be a constant: $v_0 = 1.342$. We then solve numerically the reaction-diffusion equations with the zero Neumann boundary conditions. Figure 4.1 (a) shows the cell region bounded by the blue curve. The red region inside the cell is the set of points at which the initial random concentration value $u_0 \geq 0.5$. Figure 4.1 (b) shows the part of the cell region, marked by the closed red curve, at which the concentration $u \geq 0.5$. This shows that the cell is polarized at this (rescaled) time t = 0.5. As discussed in [11,21], the reaction-diffusion system tends to minimize the length of the interface that separates the high and low u-concentration regions. Figure 4.1 (c) shows that at t = 2 the interface between the high and low u-concentration regions does not change, indicating the cell polarization reaches an equilibrium [33].

External stimulus. We introduce an external stimulus and solve the system of equations

$$\partial_t u = D_u \Delta u + f(u, v) + Sv \text{ in } \Omega^+ \times (0, T],$$

 $\partial_t v = D_v \Delta v - f(u, v) - Sv \text{ in } \Omega^+ \times (0, T],$

with the same boundary conditions $\partial_n u = \partial_n v = 0$ on $\partial \Omega^+$ and a final simulation time T. The stimulus function is Sv with S defined on $\Omega^+ \times [0, T]$ by

$$S = S(x, y, t) = \begin{cases} s_1(t)(x - 0.7)(y - 1.3) & \text{if } (x, y, t) \in \Omega^+ \times [0, 1], \\ s_2(t)(x + 0.7)(y + 1.3) & \text{if } (x, y, t) \in \Omega^+ \times [10, 11], \\ 0 & \text{elsewhere,} \end{cases}$$

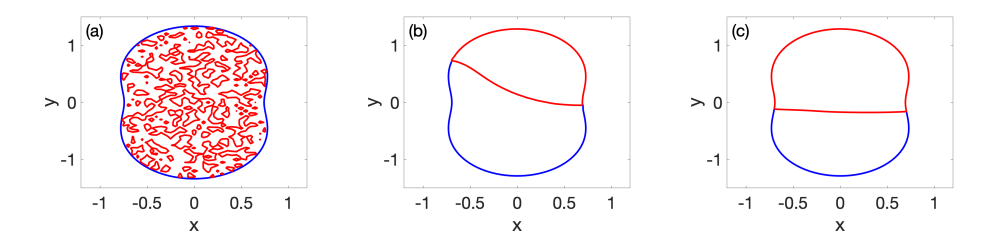


Figure 4.1: Cell polarization with a random initial value u_0 . (a) Cell region bounded by the blue curve. A random initial concentration field u_0 is distributed at grid points inside the cell region. Red spot is the set of points at which $u_0 \geq 0.5$. (b) At t = 0.5, the region of $u \geq 0.5$, bounded by the red curves, is located in the front of the cell, showing a polarized cell. (c) At t = 2, the cell polarization has reached an equilibrium.

where

$$s_1(t) = \begin{cases} 0.07 & \text{if } 0 \le t \le 0.5, \\ 0.07(1 - \frac{t - 0.5}{0.5}) & \text{if } 0.5 < t \le 1, \\ 0 & \text{elsewhere,} \end{cases} \text{ and } s_2(t) = \begin{cases} s_1(t - 10) & \text{if } 10 \le t \le 11, \\ 0 & \text{elsewhere.} \end{cases}$$

Note that the stimulus is turned on (i.e., $S(x, y, t) \neq 0$) for $0 \leq t \leq 1$, spatially weak around (x, y) = (0.7, 1.3), and for $10 \leq t \leq 11$, spatially weak around (x, y) = (-0.7, -1.3), but is turned off (i.e., S(x, y, t) = 0) for a longer period 1 < t < 10.

We set the initial values of u and v to be constant and solve the reaction-diffusion equations with the stimulus up to the final simulation time T=20. When the locally strong stimulus is turned on from t=0 to t=1, the active form u increases locally near the south-west corner. Such increase then leads to the formation of a spatial interface in the cell, separating the high and low concentrations of the active form u, that propagates inside the cell region. Meanwhile, the concentration v of the inactive form decreases, leading accordingly to the decreasing of $u^+ = Cv$ in the kinetic form of f. As a result, the motion of the internal interface slows down, and is finally pinned down, and the cell reaches a polarized steady state [33]. Figure 4.2 (a) shows such a polarized state at t=10. The cell is re-polarized, with a reversed orientation, after the stimulus is turned on again during $10 \le t \le 11$ but strong in a different spatial region of the cell; cf. Figure 4.2 (b).

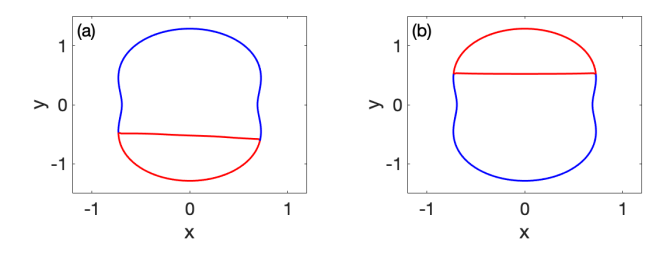


Figure 4.2: Simulation of the cell polarization with stimulus from the initial time t = 0 to the final simulation time T = 20. (a) At t = 10, the cell is polarized. (b) At t = 20, the cell is polarized again but with a reversed orientation.

4.3 Cell Trajectory

We define the cell trajectory of a moving cell to be the time trajectory of the geometrical center of the cell $(X_c(t), Y_c(t))$, which is defined by

$$X_{\mathrm{c}}(t) = \frac{1}{\operatorname{Area}\left(\Omega^{+}(t)\right)} \int_{\Omega^{+}(t)} x \, dx dy \quad \text{and} \quad Y_{\mathrm{c}}(t) = \frac{1}{\operatorname{Area}\left(\Omega^{+}(t)\right)} \int_{\Omega^{+}(t)} y \, dx dy.$$

We study two typical types of trajectories, straight and circular trajectories, aiming at a qualitative understanding of controlling parameters for such trajectories. We shall also compare the two-species and one-species models in terms of the prediction of different trajectories.

In all the simulations reported below, K = 100, M = 6, C = 0.8, and all D_u , D_v , χ , and μ^* are varied. The computational box is $\Omega = (-3,3) \times (-3,3)$ but it will be shifted during the simulation of cell movement; cf. the algorithm in section 3. The grid size is h = 0.06 and the time step size is $\Delta t = 0.005$. The initial cell boundary is a circle of radius 1.3 centered at (0,-1), The cell is polarized with the concentration of u to be 0.8, where $y \ge -0.8$, and u = 0 in the remaining part, while v is uniformly distributed on the cell domain.

Long-time trajectories. We simulate a moving cell with two different sets of parameters D_u , D_v , χ , and μ^* , and plot the cell trajectories in Figure 4.3. We observe clearly a straight trajectory (cf. Figure 4.3 (a) and (b)) and a circular trajectory (cf. Figure 4.3 (c) and (d)). Note that the parameters we use in these simulations are similar to those used in [11] to capture both the straight and circular trajectories as in Figure 4.3 with the final time t = 40 while here we have simulated the cell movement up to t = 150, indicating that the two patterns are persistent, and the model and our methods are robust.

Effects of diffusion. We now set $\chi=0.1$ and $u^*=0.4$, and vary the diffusion constants D_u and D_v to study how the diffusion can affect the cell movement. In Figure 4.4, we plot our simulation results for three sets of diffusion constants: case 1: $D_u=0.1$ and $D_v=10$; case 2: $D_u=0.3$ and $D_v=30$; case 3: $D_u=0.5$ and $D_v=50$. In Figure 4.4 (a), we observe that the cell trajectory is linear (i.e., straight) for case 1, while it is circular for case 2 and case 3. Note that the plot in the window is the zoom-in of the long-time trajectories for case 2 and case 3. In all the three cases, there is a preparation time before the cell starts to move in a straight line for case 1 or in a circular pattern for case 2 and case 3. In Figure 4.4 (b1)–(b3), we plot the x and y components of the velocity at the geometrical center of the moving cell corresponding to the three cases, respectively. We observe that larger diffusion constants correspond to a shorter preparation time before the onset of the linear or circular trajectory. Moreover, fast diffusion is correlated to a smaller circular trajectory.

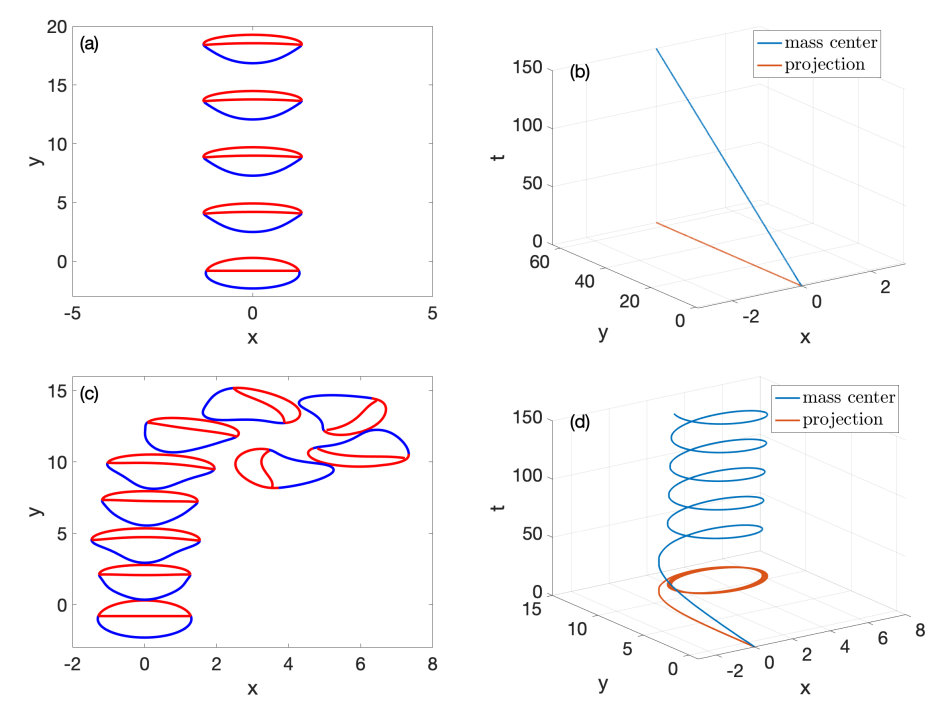


Figure 4.3: Long-time cell movement simulations. In (a) and (b), $D_u = 0.1$, $D_v = 10$, $\chi = 0.2$, and $u^* = 0.2$. In (c) and (d), $D_u = 0.5$, $D_v = 50$, $\chi = 0.1$, and $u^* = 0.25$. The sequence of snapshots of cells in (a) are taken at t = 0, 10, 20, 30, 40 and those in (c) are taken at t = 0, 5, 10, 15, 20, 25, 30, 35, 40, 45. The blue line or curve in (b) or (d) is the space-time cell trajectory, while the red line or curve in (b) or (d), marked "projection" is the (two-dimensional) space trajectory of the moving cell.

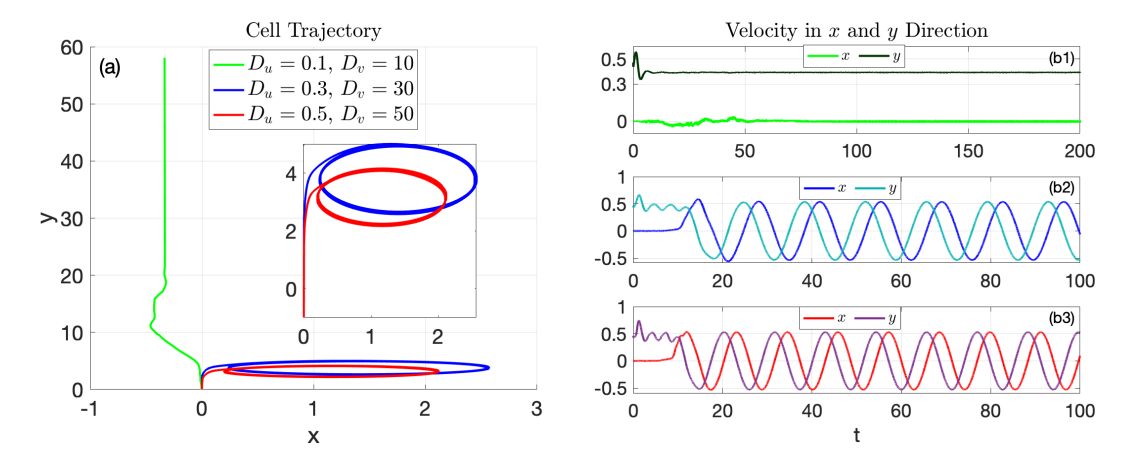


Figure 4.4: (a) Cell trajectories predicted with three different sets of diffusion constants D_u and D_v . The small window is the zoom-in of the two circular trajectories. (b1)–(b3) The x and y components of the velocity at the center of a moving cell predicted by our numerical simulations corresponding to the three sets of D_u and D_v values marked in (a).

Contractility. This refers to the cell contraction due to the decreasing of concentration u the rear part of the cell. In the model, the cell contractility is determined by the threshold concentration u^* . To study how the variation of u^* can affect the cell trajectory, we fix the diffusion constants

 $D_u = 0.4$ and $D_v = 40$ and the rescaled surface tension constant $\chi = 0.1$, and simulate the cell movement with different values of u^* : 0.25, 0.3, and 0.4. Figure 4.5 (a) shows the three circular trajectories corresponding to the three u^* values. We observe that a larger value of u^* corresponds to an earlier onset of the circular mode and the circle is smaller. Figure 4.5 (b1)–(b3) show the area of the moving cell vs. time for the three sets of u^* values as marked in Figure 4.5 (a). We observe again that a larger value of u^* takes a shorter period of time before the cell circulates.

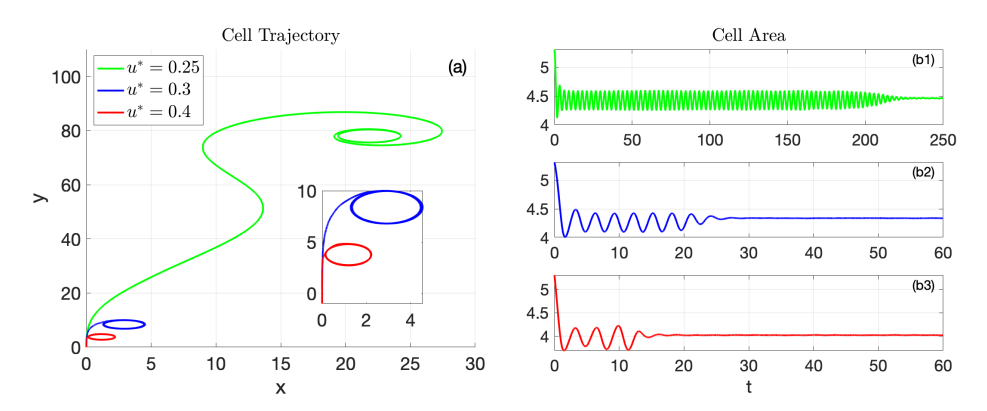


Figure 4.5: (a) Cell trajectories corresponding to the three values of u^* . (b1)–(b3) The area of the moving cell vs. time t corresponding to the three values of u^* .

Two-species model vs. one-species model. We simulate the cell movement with both the two-species model and the one-species model, in non-dimensionalized forms. The non-dimensionalized two-species model consists of Eq. (3.1)–(3.4). The non-dmensionalized one-species model consists of Eq. (1.7)–(1.9) with $\gamma = 1$, $\alpha = 1$, and β and γ replaced by u^* and χ , respectively. The function f is given by (1.5) with c = 1 and k replaced by K. We set $D_u = 0.1$, $D_v = 10$ (only for the two-species model), $u^* = 0.4$, and $\chi = 0.1$. In Figure 4.6, we plot the center of mass of the cell simulated with the two-species model (left), which predicts a linear trajectory, and the one-species model (right), which predicts a circular trajectory.

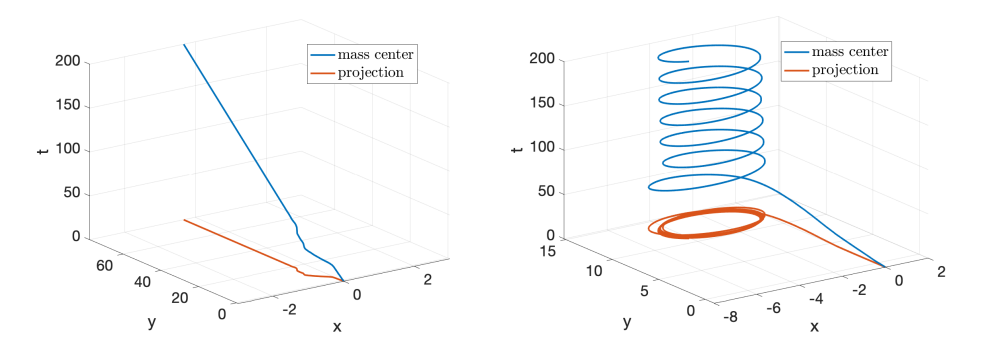


Figure 4.6: The trajectory of the center of mass of a simulated cell. (Left) A linear trajectory predicted by the two-species model. (Right) A circular trajectory predicted by the one-species model.

To see how some of the key parameters can control cell trajectories, we have simulated the cell movement with different values of the (rescaled) diffusion coefficients D_u and D_v (D_v is only for the two-species model), and the (rescaled) surface tension parameter χ . All the other parameters are the same. Our results are summarized in Table 5.

Table 5: Comparison of cell trajectories simulated by one-species (indicated by 1s) and two-species (indicated by 2s) models. The symbol "O" represents a circular trajectory, "|" represents a linear trajectory, and "×" means that cell loses polarity and stays still during the movement.

Diffusion Coefficients		$\chi = 0.1$		$\chi = 0.15$		$\chi=0.2$		$\chi = 0.25$		$\chi = 0.3$	
		2s	1s	2s	1s	2s	1s	2s	1s	2s	
$D_u = 0.10$, and $D_v = 10$ for 2s	0										
$D_u = 0.15$, and $D_v = 15$ for 2s	0	0	0		0				×	×	
$D_u = 0.20$, and $D_v = 20$ for 2s	0	0	0	0	0	0	0		×	×	

It is clear that the combination of the diffusion of active Rho GTPase proteins with the concentration u and the surface tension with the parameter χ controls the trajectory pattern, linear or circular. A large value of χ corresponds to a large surface tension and small friction, suppressing the boundary instability during the cell movement, while a larger value of the diffusion coefficient D_u causes more likely the cell circular motion. Similarly, the one-species model with the infinitely fast diffusion of the inactive Rho GTPase proteins predicts more likely a circular than a linear trajectory of the cell motion.

5 Conclusions

We have studied the cell polarity and movement within the modeling framework of reaction-diffusion equations and a moving cell boundary. In particular, we have carefully examined the wave-pinning model, both the two-species and the reduced one-species model.

Early studies included the one-dimensional analysis of the wave pinning mechanism [33,34] and the two-dimensional phase-field simulation and the sharp-interface analysis with a reduced model for cell polarization and movement [11]. Here, we have derived the sharp-interface model as the limit of the phase-field model as the small parameter $\varepsilon \to 0$ with a general two or three-dimensional setting. Our rigorous analysis provides a close link between these two types of models.

We have also developed and implemented a robust numerical method for the simulation of cell polarization and movement using the derived sharp-interface model in two-dimensional space. Our approach combines the level-set method for the moving cell boundary and accurate discretization techniques for solving the reaction-diffusion equations on the moving cell region. The method and algorithm pass the convergence test.

We have done extensive numerical simulations using the full, two-species reaction-diffusion moving cell boundary model as well as its reduced one-species model in two-dimensional space. We find that the cell polarization is a robust process that can be triggered by various external stimulus with a large set of parameters, confirming the wave-pinning mechanism as proposed in [33, 34]. We have also traced the cell trajectory during long-time simulations. By choosing different set of parameters of the diffusion constants and the threshold value of the concentration of an active Rho GTPase protein in the normal velocity, we have been able to capture both the linear and circular trajectories. It is consistently observed that a larger value of the (rescaled) diffusion constant leads more likely to a circular motion of the cell, and a larger value of the (rescaled) surface tension leads more likely to a linear motion of the cell. These agree with the qualitative analysis by Camley et al. [11]. For a circular trajectory, a period of preparation time is observed. The full, two-species model and the reduced, single-species model predict different such preparation times. Therefore, the infinite diffusion of the second species which is the assumption of the reduced model, may need to be corrected for quantitative predictions of different complex processes of cell motility.

In our simulations we have observed that the cell area and the x and y components of the velocity at center of mass of the cell to be oscillatory during the period of preparation time before the cell starts to rotate completely; cf. Figure 4.4 and Figure 4.5. These are unlikely caused by numerical errors and instabilities as no such oscillations occur once the cell starts to rotate. We will investigate such oscillations further in our subsequent works.

With our analytical tools, robust numerical methods, and computer code, we can study further the cell polarity and movement in several directions.

- (1) We can include many more biological components in our models and simulations. The first of them is the fluid flow which can be modeled by Stokes flow [43,52]. The boundary velocity of a cell moving around within such a flow can be determined by the force balance. The second component is the combination of attachment to and detachment from a substrate of a moving cell [43].
- (2) With a similar approach and simulation method, we can study the interaction and movement of a cluster of cells, where the cell coordination and cooperation will be crucial [8,40]. Likely, such studies can help understand better the molecular basis as well as mechanical forces that determine such an important collective biological process.
- (3) With our current work on the model analysis and the development of robust numerical methods for two-dimensional simulations, it is possible now for us to simulate the cell movement in a full, three-dimensional setting, with an extended model that include more biological effects, particularly those, such as cell-substrate interactions, that are not easily described by a two-dimensional model [12, 45].

Acknowledgments. This work was supported in part by an AMS Simons Travel Grant (SL), the US National Science Foundation through grant DMS-1913144 and DMS-2208465 (LTC & BL), and the US National Institutes of Health through grant R01GM132106 (BL). The authors thank Dr. Zirui Zhang and Professor Yanxiang Zhao for helpful discussions.

References

- [1] C. Anderson and C. Greengard. On vortex methods. SIAM J. Numer. Math, 22(3):413–440, 1985.
- [2] D. M. Anderson, G. B. McFadden, and A. A. Wheeler. Diffuse-interface methods in fluid mechanics. *Ann. Rev. Fluid Mech.*, 30:139–165, 1998.
- [3] L. Berlyand, M. Potomkin, and V. Rybalko. Phase-field model of cell motility: Traveling waves and sharp interface limit. C. R. Acad. Sci. Paris, Ser. I, 354:986–992, 2016.
- [4] T. Biben, K. Kassner, and C. Misbah. Phase-field approach to three-dimensional vesicle dynamics. *Phys. Rev. E*, 72:041921, 2005.
- [5] W. J. Boettinger, J. A. Warren, C. Beckermann, and A. Karma. Phase-field simulation of solidification. *Annu. Rev. Materials Res.*, 32:163–194, 2002.
- [6] N. Bolle and M. S. Mizuhara. Dynamics of a cell motility model near the sharp interface limit. J. Theo. Biol, 505:110420, 2020.
- [7] D. Bray. Cell Movements: From Molecules to Motility. Garland Science, 2001.
- [8] A. Buttenschön and L. Edelstein-Keshet. Bridging from single to collective cell migration: A review of models and links to experiments. *PLoS Comput. Biol.*, 16(12):e1008411, 2020.

- [9] B. A. Camley, Y. Zhang, Y. Zhao, B. Li, E. Ben Jacob, H. Levine, and W.-J. Rappel. Polarity mechanisms like contact inhibition of locomotion regulate persistent rotational motion of mammalian cells on micropatterns. *Proc. Natl Acad. Sci. USA*, 111(41):14770–14775, 2014.
- [10] B. A. Camley, Y. Zhao, B. Li, H. Levine, and W.-J. Rappel. Periodic migration in a physical model of cells on micropatterns. *Phys. Rev. Lett.*, 111:158102, 2013.
- [11] B. A. Camley, Y. Zhao, B. Li, H. Levine, and W.-J. Rappel. Crawling and turning in a minimal reaction-diffusion cell motility model: coupling cell shape and biochemistry. *Phys. Rev. E*, 95(1):012401, 2017.
- [12] Y. Cao, E. Ghabache, Y. Miao, C. Niman, H. Hakozaki, S. L. Reck-Peterson, P. N. Devreotes, and W.-J. Rappel. A minimal computational model for three-dimensional cell migration. J. R. Soc. Interface, 16(161):20190619, 2019.
- [13] J. B. Collins and H. Levine. Diffuse interface model of diffusion-limited crystal growth. *Phys. Rev. B*, 31:6119–6122, 1985.
- [14] R. Cortez. The method of regularized Stokeslets. SIAM J. Sci. Comput., 23(4):1204–1225, 2001.
- [15] D. Cusseddu, L. Edelstein-Keshet, J. A. Mackenzie, S. Portet, and A. Madzvamuse. A coupled bulk-surface model for cell polarisation. J. Theor. Biol., 481:119–135, 2019.
- [16] S. Dai and K. Promislow. Geometric evolution of bilayers under the functionalized Cahn–Hilliard equation. *Proc. Royal Soc. A*, 469:20120505, 2013.
- [17] K. R. Elder, M. Grant, N. Provatas, and J. M. Kosterlitz. Sharp interface limits of phase-field models. *Phys. Rev. E*, 64:021604, 2001.
- [18] P. C. Fife. Dynamics of Internal Layers and Diffusive Interfaces. SIAM, 1988.
- [19] G. H. Gilmer, W. Gilmore, J. Huang, and W. W. Webb. Diffuse interface in a critical fluid mixture. *Phys. Rev. Lett.*, 14:491–494, 1965.
- [20] G.-S. Jiang and D. Peng. Weighted ENO schemes for Hamilton–Jacobi equations. SIAM J. Scient. Comput., 21(6):2126–2143, 2000.
- [21] A. Jilkine. A wave-pinning mechanism for eukaryotic cell polarization based on Rho GTPase dynamics. PhD thesis, Univ. of British Columbia, 2009.
- [22] H. Johansen and P. Colella. A cartesian grid embedded boundary method for Poisson's equation on irregular domains. *J. Comput. Phys*, 147(1):60–85, 1998.
- [23] A. Karma, D. Kessler, and H. Levine. Phase-field model of mode III dynamic fracture. *Phys. Rev. Lett.*, 87:045501, 2001.
- [24] K. Keren, Z. Pincus, G. M. Allen, E. L. Barnhart, G. Marriott, A. Mogilner, and J. A. Theriot. Mechanism of shape determination in motile cells. *Nature*, 453:475–481, 2008.
- [25] J. S. Langer. Models of pattern formation in first-order phase transitions. In G. Grinstein and G. Mazenko, editors, Directions in Condensed Matter Physics. World Scientic, 1986.
- [26] B. Li and Y. Liu. Diffused solute-solvent interface with Poisson-Boltzmann electrostatics: Free-energy variation and sharp-interface limit. SIAM J. Appl. Math, 75(5):2072–2092, 2015.

- [27] X. Li, J. Lowengrub, A. Rätz, and A. Voigt. Solving PDEs in complex geometries: A diffuse domain approach. *Commun. Math. Sci.*, 7(1):81–107, 2009.
- [28] C. Min and F. Gibou. Geometric integration over irregular domains with application to level-set methods. *J. Comput. Phys*, 226(2):1432–1443, 2007.
- [29] C. Min and Frédéric Gibou. A second order accurate level set method on non-graded adaptive cartesian grids. *J. Comput. Phys.*, 225:300–321, 2007.
- [30] L. Modica. The gradient theory of phase transitions and the minimal interface criterion. *Arch. Rational Mech. Anal.*, 98:123–142, 1987.
- [31] A. Mogilner. Mathematics of cell motility: have we got its number? J. Math. Biol., 58:105–134, 2009.
- [32] A. Mogilner, J. Allard, and R. Wollman. Cell polarity: Quantitative modeling as a tool in cell biology. *Science*, 336:175–179, 2012.
- [33] Y. Mori, A. Jilkine, and L. Edelstein-Keshet. Wave-pinning and cell polarity from a bistable reaction-diffusion system. *Biophys. J*, 94(9):3684–3697, 2008.
- [34] Y. Mori, A. Jilkine, and L. Edelstein-Keshet. Asymptotic and bifurcation analysis of wave-pinning in a reaction-diffusion model for cell polarization. *SIAM J. Appl. Math.*, 71(4):1401–1427, 2011.
- [35] S. Osher and R. Fedkiw. Level Sets and Dynamic Implicit Surfaces. Springer-Verlag, 2002.
- [36] S. Osher and J. A. Sethian. Fronts propagating with curvature dependent speed: Algorithms based on Hamilton–Jacobi formulations. *J. Comput. Phys.*, 169(1):12–49, 1988.
- [37] S. Osher and C.-W. Shu. High order essentially non-oscillatory schemes for Hamilton-Jacobi equations. SINUM, 28:907–922, 1991.
- [38] J. Papac, F. Gibou, and C. Ratsch. Efficient symmetric discretization for the Poisson, heat and stefan-type problems with robin boundary conditions. J. Comput. Phys., 229(3):875–889, 2010.
- [39] R. L. Pego. Front migration in the nonlinear Cahn-Hilliard equation. *Proc. Roy. Soc. London Ser. A*, 422:261–278, 1989.
- [40] W.-J. Rappel and L. Edelstein-Keshet. Mechanisms of cell polarization. Curr. Opinion Systems Biol., 3:43–53, 2017.
- [41] B. Rubinstein, K. Jacobson, and A. Mogilner. Multiscale two-dimensional modeling of a motile simple-shaped cell. SIAM Multiscale Model and Simul., 3(2):413–439, 2005.
- [42] J. Rubinstein, P. Sternberg, and J. B. Keller. Fast reaction, slow diffusion, and curve shortening. SIAM J. Appl. Math., 49(1):116–133, 1989.
- [43] D. Shao, H. Levine, and W.-J. Rappel. Coupling actin flow, adhesion, and morphology in a computational cell motility model. *Proc. Natl Acad. Sci. USA*, 109(18):6851–6856, 2012.
- [44] D. Shao, W.-J. Rappel, and H. Levine. Computational model for cell morphodynamics. *Phys. Rev. Lett.*, 105:108104, 2010.

- [45] A. R. Singha, T. Leadbetterb, and B. A. Camley. Sensing the shape of a cell with reaction diffusion and energy minimization. *Proc. Natl Acad. Sci. USA*, 119(31):e2121302119, 2022.
- [46] P. Smereka. Semi-implicit level set methods for curvature and surface diffusion motion. *J. Sci. Comput.*, 5(2):257–266, 2003.
- [47] P. Sternberg. The effect of a singular perturbation on nonconvex variational problems. *Arch. Rational Mech. Anal.*, 101:209–260, 1988.
- [48] H. Sun, J. Wen, Y. Zhao, B. Li, and J. A. McCammon. A self-consistent phase-field approach to implicit solvation of charged molecules with Poisson–Boltzmann electrostatics. *J. Chem. Phys.*, 143:243110, 2015.
- [49] M. Sussman, P. Smereka, and S. Osher. A level set method for computing solutions to incompressible two-phase flow. *J. Comput. Phys.*, 114:146–159, 1994.
- [50] K. E. Teigen, X. Li, J. Lowengrub, F. Wang, and A. Voigt. A diffuse-interface approach for modeling transport, diffusion and adsorption/desorption of material quantities on a deformable interface. *Commun. Math. Sci.*, 7(4):1009–1037, 2009.
- [51] Y.-H. R. Tsai, L.-T. Cheng, S. Osher, and H.-K. Zhao. Fast sweeping algorithms for a class of Hamilton–Jacobi equations. *SIAM J. Numer. Anal.*, 41(2):673–694, 2003.
- [52] B. Vanderlei, J. J. Feng, and L. Edelstein-Keshet. A computational model of cell polarization and motility coupling mechanics and biochemistry. *SIAM Multiscale Model and Simul.*, 9(4):1420–1443, 2011.
- [53] H.-K. Zhao. A fast sweeping method for Eikonal equations. *Math. Comp.*, 74(250):603–627, 2005.
- [54] F. Ziebert and I. S. Aranson. Effects of adhesion dynamics and substrate compliance on the shape and motility of crawling cells. *PLoS ONE*, 8(5):e64511, 2013.